Probing of the non-innocent role of P in transition-metal phosphide HER electrocatalysts via replacement with electropositive Si

Seongyoung Kong,[a,b] Prashant Singh,[b] Georgiy Akopov,[a,b,g] Dapeng Jing,[c] Ryan Davis,[d] Jorge Perez-Aguilar,[d] Jiyun Hong,[d] Shannon J. Lee,[a,b,h] Gayatri Viswanathan,[a,b] Ernesto Soto,[a,b] Muhammad Azhan,[a,b] Tiago Fernandes,[f] Stasia Harycki,[a] Alexander Gundlach-Graham,[a] Yury V. Kolen'ko,[f] Duane D. Johnson,[b,e] and Kirill Kovnir[a,b,*]

[a] *Department of Chemistry, Iowa State University, Ames, IA 50011, USA*

[b] *Ames National Laboratory, U.S. Department of Energy, Ames, IA 50011, USA*

[c] *The Materials Analysis Research Laboratory, Iowa State University, Ames, IA 50011, USA*

[d] *Stanford Synchrotron Radiation Lightsource, SLAC National Accelerator Laboratory, Menlo Park, CA, 94025, USA*

[e] *Department of Materials Science & Engineering, Iowa State University, Ames, IA 50011, USA*

[f] *Nanochemistry Research Group, International Iberian Nanotechnology Laboratory (INL), Braga 4715-330, Portugal.*

[g] *Department of Chemistry, Rutgers University-Newark, Newark, NJ 07102, USA.*

[h] *Condensed Matter Physics and Materials Science Department, Brookhaven National Laboratory, U.S. Department of Energy, Upton, New York 11973, USA.*

ABSTRACT

Transition-metal phosphides (*TM*P) have been identified as promising electrocatalysts for hydrogen evolution reaction (HER). Despite recent computational investigations identifying P sites as crucial for hydrogen adsorption, the main mode of optimization for *TM*Ps has been focused on changing the metal sites. To experimentally verify computational hypotheses and provide a route for HER electrocatalyst optimization via ternary compounds, we performed systematic experimental studies of structurally related $NiSi_{1-x}P_x$ phases, namely Ni_2SiP, $Ni_5Si_2P_3$, Ni_3SiP_2, and $Ni_7Si_2P_5$, which are ordered derivatives of the NiSi structure (*Pnma*, *oP*-8, MnP structure type). We found that P played a significant role in modulating HER activity in acidic electrolyte because the incorporation of P in NiSi reduced the overpotential at current density j = 10 mA/cm^2 from η_{10} = 529 mV (NiSi) to η_{10} = 97 mV (Ni_2SiP). Ni_2SiP outperformed the current state-of-the-art Ni_5P_4 electrocatalyst prepared and studied in the identical conditions both in terms of activity and stability, which is attributed to presence of covalent Ni-Si bonding in the structure. Within the family of ternary Ni-Si-P compounds, electrocatalytic activity correlates to the number of Ni-3*d* states at the Fermi energy.

INTRODUCTION

Hydrogen energy is one of the most promising solutions to the global energy crisis due to its zero-carbon emission and high energy density compared to other energy sources.[1] Hydrogen can be sustainably produced by means of water electrolysis using renewable electricity as an input. The hydrogen evolution reaction (HER) is a cathodic half-reaction of water electrolysis while the anodic half-reaction is the oxygen evolution reaction (OER). As the HER is an electrochemical reaction between the surface of the cathode and aqueous electrolyte, an electrocatalyst that constitutes the cathode plays a pivotal role in determining the overall efficiency of water electrolysis. Thus far, scarce Pt-based materials have been utilized as a standard HER electrocatalyst, making it expensive for scalable applications. So, new alternative Pt-free electrocatalysts made of earth-abundant materials are crucial for the transition to hydrogen energy.[2]

Transition-metal phosphides (TMPs) have recently been predicted and experimentally confirmed as promising HER electrocatalysts.[3,4] TMPs are highly stable in acidic environments and outperform alternative HER electrocatalysts, *e.g.*, carbides, nitrides, oxides, and chalcogenides.[5] The commonly used TMP compositions vary from 2:1 to 1:2 of metal:phosphorus ratios, which possess a balanced hydrogen adsorption energy according to Sabatier's principle.[6–8] While the metal has been regarded as the main active site, recent studies highlight the significance of P sites in TMP electrocatalysts. Namely, the P not only moderates the electronic structure of the electrocatalysts but also acts as an actual active site to adsorb H.[9–11] For example, Ni_5P_4 has better HER activity than Ni_2P because P sites exhibit near-zero hydrogen adsorption energy and Ni_5P_4 has a higher number of P sites per Ni atom.[10] Experimental studies of FeP and NiP_2 single crystals confirmed that adsorption of hydrogen on P surface sites is a general property trend.[12] Experimental reports that identify the role of P are relatively scarce.[13] Our approach here is to partially replace P with its neighboring non-metal element, Si, and investigate the properties of ternary Ni-Si-P catalysts.

The compositional phase space of binary nickel phosphides (NiP_x), the first demonstrated TMP HER electrocatalysts, is diverse, *i.e.*, Ni_3P, Ni_8P_3, Ni_5P_2, $Ni_{12}P_5$, Ni_2P, Ni_5P_4, two polymorphs of NiP_2, and NiP_3.[4,11,14–17] So far, Ni_5P_4 (Ni : P = 1.25) is the most active HER electrocatalyst among

NiP_x phases.[16] NiP (Ni : P = 1) is also expected to have high HER activity, but it is extremely challenging to synthesize in bulk form, unlike FeP or CoP.[18,19] In turn, NiSi is stable bulk phase crystallizing in the same structure type as FeP or CoP, *i.e.*, MnP structure type, *Pnma* space group, Pearson symbol *oP*-8. Partial replacement of Si with P in NiSi results in the formation of structurally-related ordered compounds with simplified formula $NiSi_{1-x}P_x$ ($x = 0.5$ Ni_2SiP, *Pbca;* $x = 0.6$ $N_5Si_2P_3$, *Pbca*; and $x = 0.714$ $Ni_7Si_2P_5$, *Pbcn*).[20–23] We hypothesized that ternary Ni–Si–P phases could be good candidates to systematically study the function of Si/P content on HER activity. Importantly, NiSi ($x = 0$) could be the reference for $NiSi_{1-x}P_x$ electrocatalyst with no P.

Electronegative non-metal elements, such as N, O, F, S, and Se, are general dopants in *TM*P electrocatalysts to promote electron transfer from the metal to anion and lower the filling of metal *d*-bands, mitigating too strong hydrogen adsorption energy of the metal sites.[24–36] However, incorporation of electropositive elements is less studied, because of fewer reported TM-P-(Al or B) phases. These studies show that Al replaces the metal sites and broadens the metal *d*-band while B replaces P sites and decreases the density of states of the metal *d*-band at Fermi energy (E_F), both balancing the hydrogen adsorption energies of the metal sites.[37–39] Si is another main group element that is more electropositive than P. However, despite many known *TM*-Si-P phases, there have been no reports on P- and Si-containing *TM*P electrocatalysts for HER. This might be due to the difficulty of functionalizing Si in the majority of synthetic routes toward *TM*P electrocatalysts.[40]

Herein, we have synthesized single-phase samples of Ni_2SiP, $N_5Si_2P_3$, and $Ni_7Si_2P_5$ through molten salt flux-assisted solid-state reactions utilizing atomically mixed precursors. Moreover, we discovered an additional member of the $NiSi_{1-x}P_x$ family - Ni_3SiP_2, $x = 0.67$. Our catalytic studies, relying on a working electrode with a dense pellet, allowed us to reduce the uncertainties associated with the synthesis of nanoparticles, particularly in underestimating the proper surface area and electrocatalytically-active surface area.[41] The electrochemical properties, stability, and bulk and surface structure of ternary $NiSi_{1-x}P_x$ phases were investigated in comparison to the NiSi and Ni_5P_4 reference binary materials prepared in identical conditions.

EXPERIMENTAL SECTION

Solid-state synthesis

Ni (99.996%) and red phosphorus (98.7%) powders from Alfa Aesar were used for solid-state syntheses. CsBr (99.8%) from Alfa Aesar and CsCl (99.99%) from Sigma Aldrich were mixed in a 1:1 weight ratio and used as a salt flux. For the arc-melted precursor, Ni pellet (99.99%) and Si lumps (99.9999996%) were acquired from the Materials Preparation Center at Ames National Laboratory, which is supported by the U.S. Department of Energy (DOE) Basic Energy Sciences. Ni–Si binary precursors were arc-melted with 100A current using the Ni:Si ratios of 1:1, 2:1, 5:2, and 3:1 for synthesis of NiSi, Ni_2SiP, $Ni_5Si_2P_3$, and Ni_3SiP_2, respectively (**Figures S1 and S2**).The resultant arc-melted ingots of Ni–Si precursors were ground into powders for further reaction with P. Due to difficulties in grinding Ni–Si precursors containing more than 75% of Ni, the Ni_3Si precursor was used for $Ni_7Si_2P_5$ synthesis with an additional stoichiometric amount of Ni powder. The prepared Ni–Si precursor, stoichiometric amounts of P, and salt flux were loaded in 9/11 mm (I.D./O.D.) silica tubes, then flame-sealed under vacuum, heated to 800 °C for 12 h, dwelled for 72 h, and naturally cooled. The total weight of reactants was 200 mg and the flux amount was 400 mg. When the reaction was finished, the ampoule was opened under ambient conditions and the product was immersed in water for 2 h to remove the flux, filtered, and dried in the air overnight. A mixture of fine dark-gray powders and lumps of the corresponding Ni–Si–P compound were obtained. Single-phase Ni_5P_4 was synthesized by using the same heating profile with stoichiometric ratio of Ni and P (300 mg of total mass) and CsCl flux (600 mg).

Spark plasma sintering

Ni–Si–P samples were pressed into a 5 mm diameter pellets by means of spark plasma sintering (SPS, Dr Sinter Lab Jr. SPS-211Lx, Sumitomo Coal Mining Co., Ltd.). About 90 mg of the sample was loaded in a 5 mm graphite die, capped by graphite sheets. Tungsten carbide (WC) plungers were used. The SPS chamber with the die inside was evacuated, and partially filled by Ar gas to avoid evaporation of phosphorus during the sintering. An initial pressure of 50 MPa was applied to the specimen at room temperature before sintering, and then the die assembly was heated to 350 °C for 5 min followed by 10 min of dwelling. After reaching the desired temperature, the pressure was increased to 200 MPa. Prior to cooling the pressure was released. The geometric pellet density was estimated to be around 70% for all sintered pellets.

Cathode fabrication

The 5 mm pressed pellets of $NiSi_{1-x}P_x$ and Ni_5P_4, and the arc-melted NiSi chunk, were connected to Cu wire by using H20E conductive epoxy (Epoxy Technology), and the assembly was transferred to a vacuum oven and dried at 150 °C for 1 h. Once the conductive Cu wire was firmly attached to the pellet, this assembly acted as a cathode for HER. Entire parts were molded with insulating epoxy to prevent the exposure of the assembly to the electrolyte. After molding, the bottom part of the cathode was polished using various grits of sandpaper (up to 1500 grit) to expose the fresh surface of the pellet. Then, it was polished using alumina dispersions with 1, 0.3, and 0.05 μm particles size. Between these polishing steps, the cathode was sonicated in water and ethanol for 5 and 3 min, respectively, to remove any polishing contaminants from the surface. A picture of the fabricated cathode is shown in **Figure S12**.

Powder X-ray diffraction (XRD)

For powder X-ray diffraction, a benchtop MiniFlex600 diffractometer (Rigaku) with Cu-K_α radiation (λ = 1.540593 Å) and a Ni-K_β filter were used. Zero-background holders were used for data collection under ambient conditions. Rietveld refinement of the obtained diffractions patterns was performed using the GSAS-II software.[42] An internal standard (Si powder, SRM 640b, NIST, a = 5.430940 Å) was utilized to obtain the accurate unit cell parameters.

Differential scanning calorimetry (DSC)

A DSC 404 F3 Pegasus (Netzsch) was used for thermal stability studies. About 20 mg of sample was placed in silica ampoule, which was evacuated and flame-sealed for the DSC measurement. An empty ampoule was used for background correction. The sample was heated to 1000 °C from room temperature with a rate of 10 °C/min and cooled down to 50 °C using the same rate.

Scanning electron microscopy (SEM) and energy dispersive X-ray spectroscopy (EDX)

Surface morphology and chemical composition analyses were conducted on Quanta 250 field emission SEM (FEI) operated at 15 kV and equipped with a X-Max 80 EDX detector (Oxford Instruments). Acquired EDX data were processed using the Aztec software package. Pressed pellets of the catalysts as-synthesized and after HER catalytic tests were analyzed by SEM/EDX.

X-ray photoelectron spectroscopy (XPS)

The XPS measurements were performed using an Amicus/ESCA 3400 instrument (Kratos). The sample was irradiated with 240 W Mg-K_α X-rays from a twin-anode lab source. Photoelectrons emitted at 0° from the surface normal were energy analyzed using a DuPont type analyzer. The pass energy was set at 150 eV and a Shirley baseline was removed from all reported spectra. The CasaXPS software package was used to process collected XPS data. All XPS spectra were corrected for charging effects by setting the binding energy of the C1s peak to 284.6 eV. Samples were prepared as pellets for XPS measurements under different conditions - right after polishing, after HER, after storage in air, and after long-term HER tests. For XPS depth profiling, ESCALAB 250 Xi (Thermo Scientific) was utilized with a monochromated micro-focused Al-K_α X-ray source and analysis spot of 650 × 400 μm^2. Ar cluster beam at 6000 eV was utilized for 10 s per cycle. The spectra were obtained under normal emission conditions using a magnetic lens that allowed for an effective analyzer collection angle of ~30°. Nominal instrument resolution of 0.36eV and step size of 0.1 eV were utilized to collect elemental regions.

X-ray absorption spectroscopy (XAS)

XAS measurements were performed at the Stanford Synchrotron Radiation Lightsource (SSRL) at SLAC National Accelerator Laboratory at beamline 11-2 using a Si(220) monochromator. X-ray absorption near edge structure (XANES) and extended X-ray absorption fine structure (EXAFS) spectra were recorded at the Ni K-edge (8333 eV) in fluorescence mode using a 100-element germanium solid-state detector array. NiSi, $NiSi_{1-x}P_x$, and Ni_5P_4 powders were smeared in between a thin layer of Kapton tape. The Athena software was used to pre-process the data including alignment, edge calibration, normalization, and background subtraction.[43] The energy at Ni *K*-edge was determined by the first inflection point of the absorption edge data when characterizing the reference nickel foil and was calibrated to the reported energy of 8333.0 eV.

Electrochemical testing

The electrochemical HER properties in acidic electrolyte were measured using a 1010E potentiostat (Gamry) with three-electrode system in degassed 0.5 M H_2SO_4 electrolyte (pH = 0). A saturated calomel electrode (SCE, Gamry) was used as the reference electrode, the aforementioned lab-made pellet-based cathode assembly was used as working electrode, and a polished and cleaned graphite rod (Gamry) was used as the counter electrode. To measure the acidic HER properties of the synthesized electrocatalysts, cyclic voltammetry (CV) was conducted with a scan rate of 5 mV/s in the potential range from –0.85 V_{SCE} to –0.25 V_{SCE} applying 100% internal resistance compensation. H_2 gas was purged for 30 min before conducting the measurement. Reported data was collected after 50 CV cycles, which were needed to achieve steady-state conditions. Measured potentials were converted to a reversible hydrogen electrode (RHE) using the following equation: $E_{RHE} = E_{SCE} + 0.244\ V + 0.059\times pH$. The reproducibility of the data was checked by studying several pellets of Ni_2SiP produced from powders synthesized in different synthetic batches. The obtained overpotentials were within 5% of each other.

Electrochemical impedance spectroscopy (EIS) analysis was measured at –0.17 V_{RHE} in the frequency range from 10^5 to 10^{-2} Hz with 5 mV AC amplitude. The solution resistance (R_u) was measured by using the point at the highest frequency of the Nyquist plot and utilized for 100% iR_u compensation of the collected electrochemical data. Charge transfer resistance (R_{ct}) was estimated by fitting the diameter of the recorded semicircle of the Nyquist plot.

To estimate double-layer capacitance (C_{dl}) of the electrocatalysts, CV curves were measured in the range from 0 V_{RHE} to 0.25 V_{RHE} with increasing scan rates: 20 mV/s, 40 mV/s, 60 mV/s, 80 mV/s, and 100 mV/s. The absolute value of current density difference at 0.15 V_{RHE} was used for calculating the C_{dl}. The electrochemically active surface area (ECSA) was further derived using an average specific capacitance value ($C_s = 35\ \mu F/cm^2$) of several metals in H_2SO_4 electrolyte.[44,45]

The stability of the cathodes was investigated by accelerated degradation testing (ADT) using CV at a scan rate of 50 mV/s recorded in the potential range from –0.65 V_{SCE} to –0.25 V_{SCE} for a continuous 1,000 cycles. Another stability testing of the cathodes was carried out by means of chronopotentiometry (CP) at the fixed current density $j = -10\ mA\ cm^{-2}$ while monitoring the variation of applied potential for continuous 20 h.

Inductively coupled plasma mass spectrometry (ICP-MS)

Ni concentrations in spent electrolyte after 3d of HER testing were determined via ICP-MS with an icpTOF-S2 (Tofwerk AG, Thun, Switzerland) equipped with a microFAST MC syringe based autosampler (Elemental Scientific, Omaha, NE, USA).

Density functional theory (DFT) calculations

DFT as implemented in Vienna *ab initio* simulation package (VASP) was used for electronic-structure calculation based on the Perdew, Burke, and Ernzerhof (PBE) exchange-correlation functionals.[46–48] Full relaxation (volume and atomic coordinates) was performed until energy and forces converged to 10^{-6} eV and 10^{-3} eV/Å, respectively. A kinetic-energy cutoff of 520 eV was used for the plane-wave basis set. Both spin-polarized and non-spin-polarized calculations were performed due to the presence of Ni, however, the Ni–Si–P system shows no spin-polarization. Monkhorst-Pack *k*-mesh grids of 4×5×6 (hypothetical NiP), 1×2×2 ($Ni_7Si_2P_5$), 2×1×2 ($Ni_5Si_2P_3$), 3×3×1 (Ni_2SiP), and 4×5×4 (NiSi) were used to sample the Brillouin zone for relaxation, while mesh-sizes were doubled for charge self-consistency, reliable formation enthalpy, and electronic-structure properties. The bonding analysis was performed using projected crystal orbital Hamilton population (pCOHP) as implemented in Local Orbital Basis Suite Towards Electronic Structure Reconstruction code (LOBSTER).[49–51] The projected COHP is a modern variant of the traditional COHP technique in which the off-site densities-of-states are weighted by the respective Hamilton matrix elements to reveal bonding, nonbonding, and antibonding interactions.[52,53]

RESULTS AND DISCUSSION

Synthesis

The reported synthetic method for $NiSi_{1-x}P_x$ is a reaction of pure elements and requires more than two weeks of annealing. The previous reports only provide single crystal data, and no specific conditions to produce single-phase powders were given.[22] From our replicate experiments using elements as starting materials, it was found that the target phases always came along with unreacted Si or unwanted binaries such as NiSi, Ni_2P, and Ni_5P_4. To avoid long synthesis times, the atomic mixing of refractive components was utilized by means of arc-melting. According to powder XRD (**Figure S1)**, the arc-melted Ni_2Si precursor was a single-phase of Ni_2Si, and the precursor with nominal Ni_5Si_2 (= $Ni_{30}Si_{12}$) composition included a dominant phase of $Ni_{31}Si_{12}$. The precursor with nominal Ni_3Si composition consisted of a mainly $Ni_{31}Si_{12}$ and an admixture of elemental Ni. Once the Ni-Si arc-melted precursors were made, they were ground into powders and further reacted with stoichiometric amounts of P in a molten salt flux at 800 °C for 3 days, producing a single-phase samples of ternary $NiSi_{1-x}P_x$. Notably, both Ni and Si elements in the arc-melted precursor actively participated in the reaction, evidenced by the absence of elemental Ni and Si or Ni-Si binaries in the products. The success of the arc-melted Ni–Si precursor relies on the idea that both refractive elements are introduced into the reaction medium with P at the same time and are both in close spatial proximity. This methodology works well for the synthesis of many complex ternary and multinary materials.[54–59] Interestingly, using the arc-melted precursor methodology, a new Ni_3SiP_2 phase was synthesized along with reported Ni_2SiP, $Ni_5Si_2P_3$, and $Ni_7Si_2P_5$ phases. Reference materials were synthesized by arc-melting for NiSi, and by the direct reaction of Ni and P in stoichiometric ratio in identical conditions to those of $NiSi_{1-x}P_x$ for Ni_5P_4 (**Figure S2**).

Structure

The powder XRD patterns of the as-synthesized Ni_2SiP, $Ni_5Si_2P_3$, Ni_3SiP_2, and $Ni_7Si_2P_5$ samples are shown in **Figure S3a** and Rietveld refinements confirm the single-phase nature of the samples (**Figure S4 and Table S1)**. All studied compounds are ordered superstructures of the parent NiSi structure, and the overall appearance of the collected XRD patterns is quite similar. Neither binary nor other admixture phases were identified. Due to the low X-ray scattering contrast between Si and P, we cannot prove the full atomic ordering of Si and P sites, as in the reported crystal structures, using powder XRD alone. Yet, these samples do exhibit a systematic shift of peak positions with changes in the nominal P content (**Figures S3b**).

Figure 1 (a) shows the refined unit cell volume of $NiSi_{1-x}P_x$ phases per Ni atom with respect to the P content. An internal NIST Si standard was used for the accurate refinement of lattice parameters. Incorporation of P into NiSi resulted in the systematic increase of the unit cell volume. Nominal and actual P content obtained from EDX are in good agreement (**Figure 1b**) which is indicative of the single-phase nature of the samples. The EDX compositions normalized by the expected Si content were estimated to be $Ni_{2.3(2)}SiP_{0.97(3)}$, $Ni_{4.8(2)}Si_2P_{2.86(6)}$, $Ni_{3.1(1)}SiP_{1.91(9)}$, and $Ni_{6.9(5)}Si_2P_{4.9(1)}$ (**Figure S6-S8**). Differential scanning calorimetry (DSC) results showed that $NiSi_{1-x}P_x$ phases decompose or melt with an onset temperature of ~840°C (**Figure S9**). A major endothermic peak with little shoulder and two exothermic peaks may indicate the peritectic decomposition of ternary $NiSi_{1-x}P_x$ phases. DSC results show that the $NiSi_{1-x}P_x$ phases are stable at the temperature used for sample densification via SPS, 350°C.

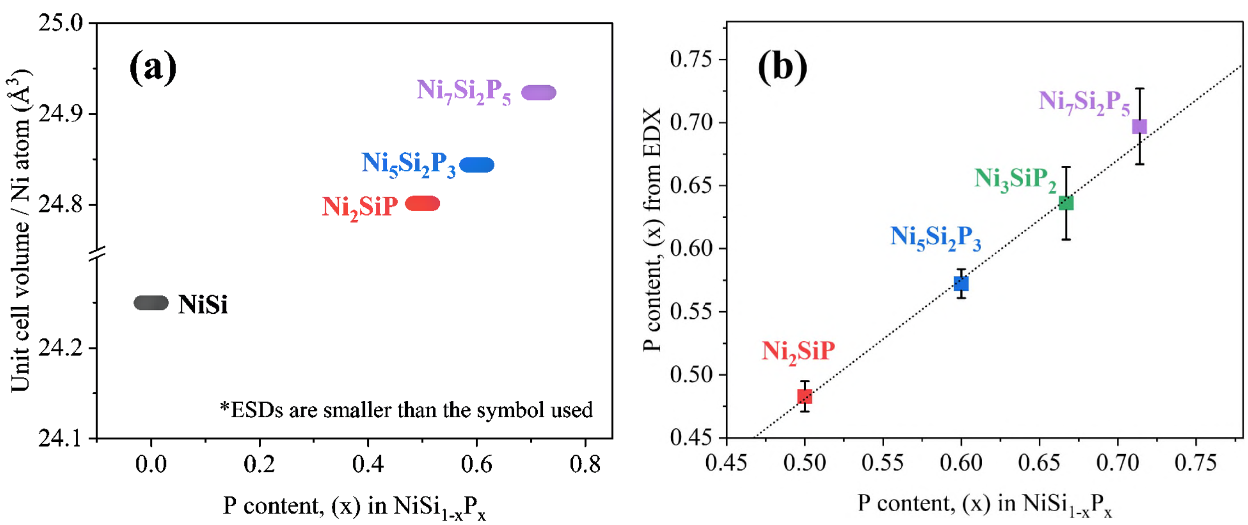

Figure 1. (a) Unit cell volume obtained from Rietveld refinement (normalized to the number of Ni atoms) and (b) experimental P content obtained from energy dispersive X-ray spectroscopy (EDX) versus nominal P content. Due to the lack of a Ni_3SiP_2 crystal structure, the unit cell volume from phase refinement is not shown. Estimated standard deviations (ESDs) of the unit cell volume in (a) are smaller than than the size of the symbol in the plot.

To analyze the surface of the electrocatalysts before and after acidic HER testing, XPS studies were conducted (**Figures 2a-e and S10**). All spectra were energy-calibrated by adjusting the measured adventitious carbon C 1s peak position at 285.0 eV. O 1s spectra are not shown, but O was detected on the surface of every sample. The sintered $NiSi_{1-x}P_x$ cathode pellets were prepared independently to be probed under four different conditions: (*i*) fresh surface right after cathode polishing (bottom row), (*ii*) after 3 days of acidic HER testing while conducting 50 CV cycles per day (second from bottom row), (*iii*) after storing as-synthesized samples in air for 30 days (third from bottom row), and (*iv*) after accelerated degradation testing (ADT) in acidic HER for 1,000 cycles (top row).

The XPS spectra for Ni $2p_{3/2}$ and P 2p indicated that the binary Ni_5P_4 (**Figures 2d-e**) displayed surface chemistry typically seen in freshly prepared metal phosphides. The spectra revealed the presence of some covalent bonding, exhibiting a formal oxidation state close to 0, with Ni at 853.3 eV, and P at 129.2 eV ($2p_{3/2}$) and 130.2 eV ($2p_{1/2}$), and oxidized ones for Ni^{2+} and P^{5+} at significantly higher binding energies, 855.8 and 133.8 eV, respectively. Ni $2p_{3/2}$ spectra at higher energies (< 860 eV) represented satellite peaks. The binding energy of 853.3 eV, which is higher than that of metallic Ni (852.6 eV), suggested positively charged Ni that transferred electrons to P.[13,60,61] After 150 cycles of acidic HER over 3 days, oxide peaks became more pronounced, which indicates that the major component of the surface is oxide. When fresh sample was stored in air for 30 days, oxide peaks increased but the degree of oxidation was less than the sample after HER testing for 3 days. Finally, after 1,000 cycles of ADT stability testing, the surface of the studied Ni_5P_4 was fully oxidized.

For ternary Ni_2SiP (**Figures 2a–c**), a similar behavior was observed. The freshly prepared sample had similar content of the covalent and oxidized Ni and P components to Ni_5P_4 as Ni $2p_{3/2}$ spectra showed main peaks at 853.3 and 856.1 eV and P 2p showed 129.8 and 134.1 eV. After 150 CV cycles in acidic HER, the surface of the sample was moderately oxidized but when the fresh sample was stored in air, it caused a dominantly oxidized surface, which is consistently shown in the rest of $NiSi_{1-x}P_x$ electrocatalysts (**Figure S10**). Prolonged cycling during ADT testing resulted in a sample which had no covalent P components but still had some covalent Ni component, which was not the case for Si-free binary Ni_5P_4. Similar resistance to oxidation of the Ni component from HER measurements was found for the rest of $NiSi_{1-x}P_x$ electrocatalysts, indicating that the presence of Ni–Si covalent bonding makes ternary compounds more resistant to full oxidation of their surface. Si 2p XPS spectra of Ni_2SiP followed the general trend, with substantial presence of the covalent Si component (99.4 eV and 101.0 eV) in freshly prepared sample, which was later suppressed after extensive ADT stability cycling (**Figure 2c**).[62,63] Other $NiSi_{1-x}P_x$ electrocatalysts displayed similar XPS spectra trends with the exception of the Si 2p signal obseved in $Ni_5Si_2P_3$ and $Ni_7Si_2P_5$, wherein covalent Si peaks intensified after 150 and 1000 cycles testing (**Figure S10**). Further XPS depth profiling for Ni_2SiP electrocatalyst showed that as ethching proceeded, the metallic component of Ni, P, and Si were partially restored, indicating the presence of oxidized phases as the thin surface layer which can be reduced back to covalent silicon-phosphide (**Figure S11**). The depth profiling results agree with similar studies for other Ni-P catalysts, such as NiP_2.[13]

The observed oxide phase may be generated either *in situ* during the HER reaction (implying that the oxide is an active site) or after the reductive bias is removed (implying that the reduced suface is oxidized by the sulfuric acid electrolyte and oxygen from the air). Formation of the *in situ* oxide phase in the reducing HER environment with an applied voltage bias and the generated hydrogen is not very probable. Moreover, if the oxide phase is an active electrocatalysts, the as-synthesized Ni_2SiP sample that was stored in air for 30 days should develop such an oxidized surface shell and is expected to be more active. However, the electrochemical HER activity of the fresh Ni_2SiP samples and those stored for 30 days were comparable, with stored the sample exhibiting lower activity, i.e. higher overpotentials (**Figure S16**). This indicates that the surface oxide most likely is not responsible for the HER activity of the electrocatalyst. Thus, we hypothesize that the formation of the oxide surface happens upon exposure of the reduced active surface to acid and air, *i.e.*, after the acidic HER reaction was finished.[64]

To better understand the oxidation states of Ni, Ni *K*-edge XAS data were collected from NiSi, $NiSi_{1-x}P_x$, and Ni_5P_4 electrocatalysts. In **Figure 2f**, the XANES results showed that Ni_5P_4 had the highest pre-edge intensity (before 8340 eV) while the pre-edge intensities of NiSi and Ni_2SiP were slightly lower. The observed spectra of Ni_5P_4 and NiSi at around 8333 eV agreed with the previously reported data, and the nearly identical pre-edge positions of Ni_2SiP and NiSi indicates similar Ni oxidation states in both compounds. In line with the XPS observations, the Ni electronic states in NiSi and $NiSi_{1-x}P_x$ are sligtly different from that of elemental Ni, as can be seen from the plot of 1st derivative of XANES data (**Figure S12**).[65–67]

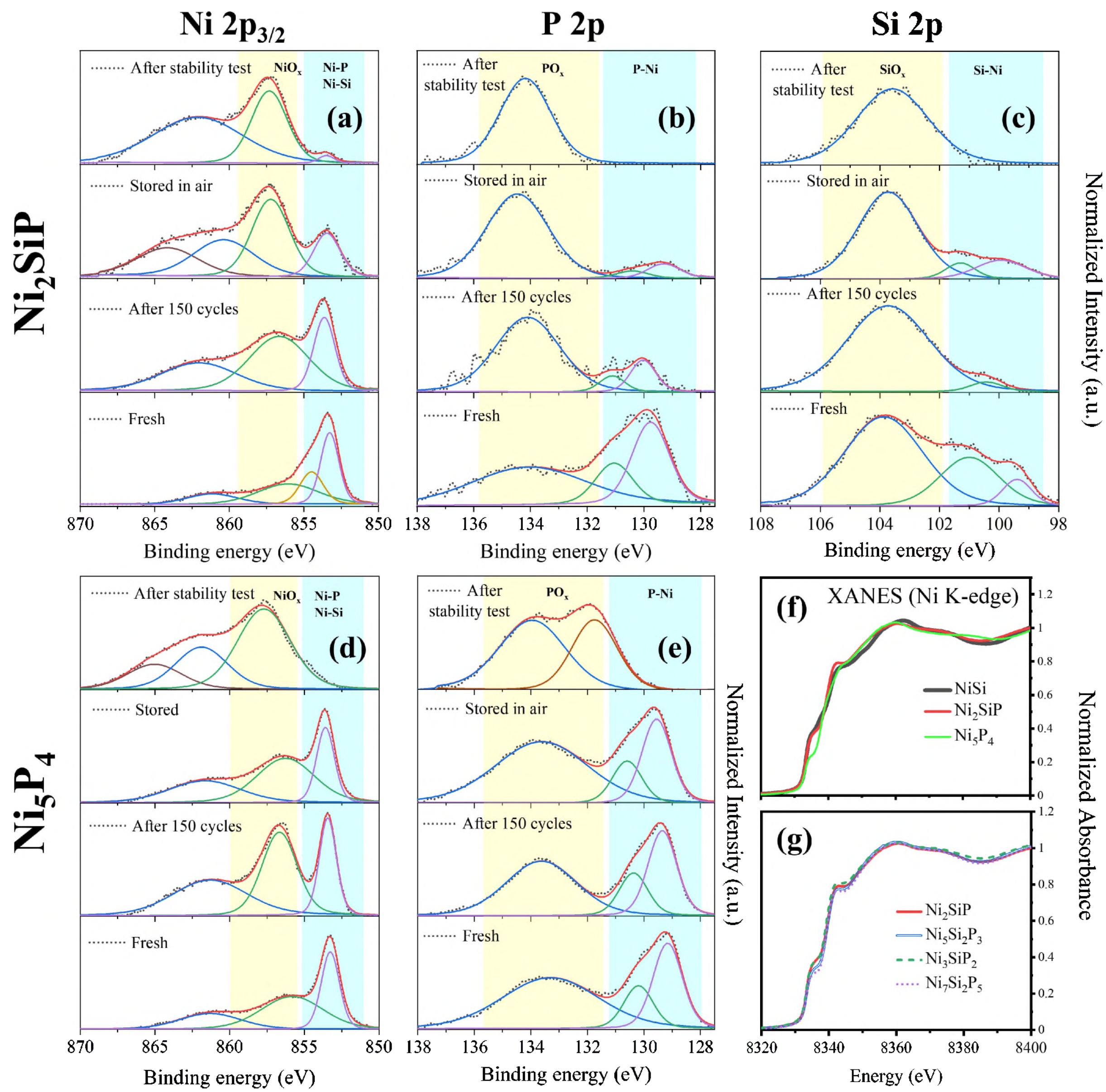

Figure 2. (a–e) High-resolution XPS data for the electrocatyalysts before and after acidic HER: (a) Ni $2p_{3/2}$, (b) P 2p, and (c) Si 2p of Ni_2SiP, as well as (d) Ni $2p_{3/2}$ and (e) P 2p of Ni_5P_4. In each panel, the spectra in bottom row are for fresh cathodes just after polishing; the spectra in second from bottom row are for the electrocatalysts after 150 CV cycles in acidic HER during 3 days; the spectra in third from bottom row are for the cathodes stored in air for 30 days; and the spectra in the top row are collected after ADT stability testing. The corresponding labels for the components are provided on the top of each panel. Symbols: raw data; red lines: overall fits; colored lines: deconvoluted fits of individual components. Ni *K*-edge XANES of (f) NiSi, Ni_2SiP, and Ni_5P_4 and of (g) the four $NiSi_{1-x}P_x$ electrocatalysts.

In **Figure 2g**, the Ni K-edge of the XANES spectra of all four $NiSi_{1-x}P_x$ phases showed similar Ni oxidation states based on the pre-edges positioned at around 8333 eV. Thus, one can conclude that the observed drastic difference in electrochemical HER activities of binary NiSi and ternary Ni-Si-P compounds (*vide infra*) is not due to the substantial alternation of the Ni oxidation state in the silicide when compared to silicon-phosphides. Rather, it should be related to the presence of P in the active HER electrocatalysts. The analysis of the k^3-weighted Fourier-transformed EXAFS (**Figure S13a and Table S2)** showed that average Ni-Si/P and Ni-Ni distances in Ni_2SiP and Ni_5P_4 are shorter than that in NiSi, which agrees with the reported crystal structures.[20,68] For the family of four $NiSi_{1-x}P_x$ phases, the average interatomic Ni-Si/P and Ni-Ni distances are similar which is expected for ordered derivatives of the same crystal structure (**Figure S13b)**.

Electrochemical analysis

All working electrodes were prepared in the same manner as described in the experimental section, namely, the consolidation of as-synthesized single-phase NiSi, $NiSi_{1-x}P_x$, and Ni_5P_4 powders into dense pellets by means of SPS, connecting pellets to the conductive Cu wire, molding in epoxy, and finally polishing the surface of the cathode to be exposed (**Figure S14**). The SEM images showed that the polished surface of the prepared working electrode was dense and flat (**Figure S8**). Cyclic voltammetry was conducted for each $NiSi_{1-x}P_x$ cathode to measure the HER activity in the 0.5M H_2SO_4 electrolyte (pH = 0) after purging with H_2 for 30 min. The scan rate was 5mV/s and iR_u was compensated in each measurement. Every measurement was recorded after the 50 CV cycles needed for the stabilization of the electrochemical system. **Figure 3a** shows the cathodic polarization curves of the NiSi, $NiSi_{1-x}P_x$, and Ni_5P_4 electrocatalysts. An η_{10} value represents the required overpotential to generate current density j = 10 mA/cm^2 as an estimate for evaluating the HER activity of the electrocatalysts. When x = 0 (*i.e.*, no P), NiSi showed a very high overpotential η_{10} = 529 mV to reach the current density j = 10 mA/cm^2, indicating poor HER activity of nickel silicide in line with previous reports.[69,70] However, as soon as 50% of Si was replaced with P, the η_{10} value of ternary Ni_2SiP was dramatically reduced to 97 mV, which is comparable to that of binary Ni_5P_4 (η_{10} = 95 mV). In this study a polished dense pellet was utilized as a cathode for both reference Ni_5P_4 and the studied ternary Ni-Si-P catalysts. The η_{10} value of Ni_5P_4 observed in this study is lower than the one in previous reports,[16] which may be related to difference in surface area, material synthesis, and measurements. In the field of HER, phosphide catalysts with a wide spread of overpotentials and Tafel slopes were reported for binary catalysts with the same nominal composition.[17] In the current work, the synthesis, processing, electrode preparation, and catalytic test conditions were kept as identical as possible for reference Ni_5P_4 and the studied ternary Ni-Si-P catalysts allowing us to make a valid conclusion regarding the relative activity of the catalysts. The commercial Pt electrode (surface area: 0.0314 cm^2) showed η_{10} = 23 mV (**Figure S15**) in the same measurement environment.

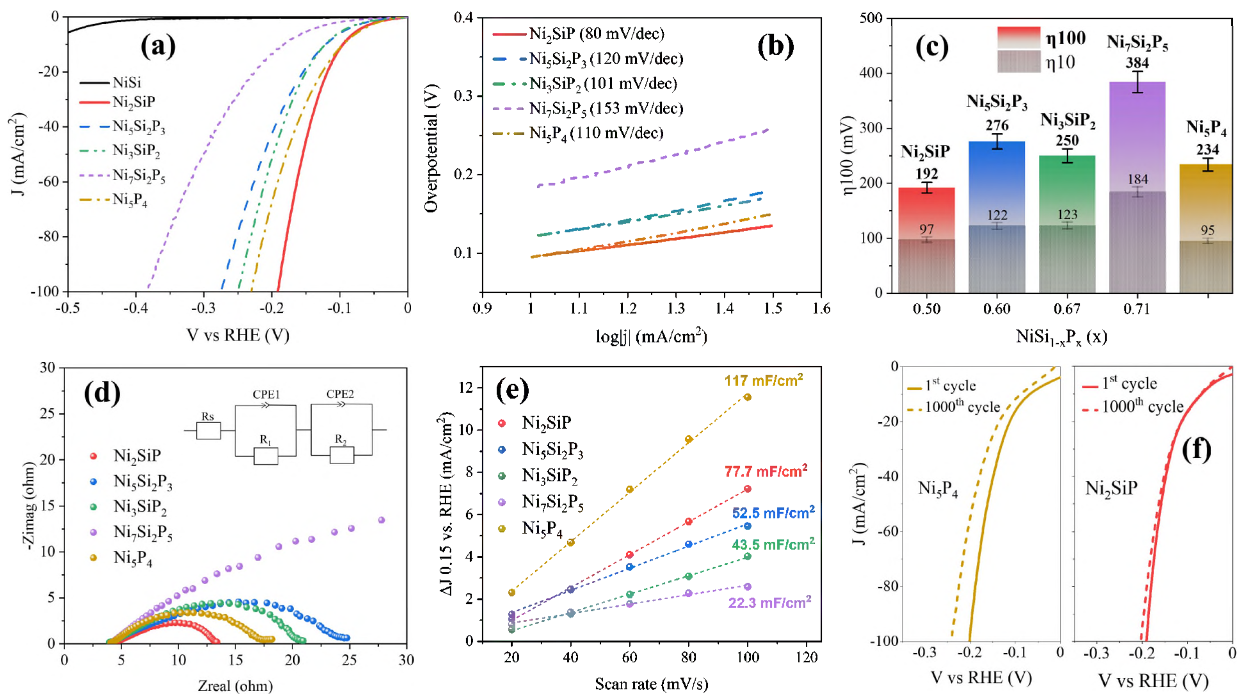

Figure 3. (a) Cathodic polarization curves, (b) Tafel slopes, (c) histograms with η_{10} and η_{100} values, (d) Nyquist plots recorded at –0.17 V_{RHE}, and (e) geometric double-layer capacitance plots for NiSi, Ni_2SiP, $Ni_5Si_2P_3$, Ni_3SiP_2, $Ni_7Si_2P_5$, and Ni_5P_4 cathodes. (f) Cathodic polarization curves for Ni_5P_4 and Ni_2SiP before and after accelerated degradation testing (ADT) for 1,000 consecutive CV cycles. All data were recorded in 0.5 M H_2SO_4 at room temperature.

When it comes to overpotential η_{100} to reach the current density j = 100 mA/cm^2, the ternary Ni_2SiP cathode displayed superior acidic HER activity as it only required η_{100} = 192 mV while binary Ni_5P_4 cathode required η_{100} = 234 mV. Notably, the incorporation of P significantly improved the acidic HER activity of NiSi while maintaining similar bulk structural motifs. This observation is in line with the computational results suggesting that P is a crucial H adsorption site for phosphide electrocatalysts.[10] Further increasing P content in $NiSi_{1-x}P_x$ cathodes, however, was not directly proportional to the improvement of acidic HER activity, as the η_{10} values for $Ni_5Si_2P_3$, Ni_3SiP_2, and $Ni_7Si_2P_5$ were estimated to be 122, 123, and 184 mV, respectively. This trend became more pronounced for η_{100} values (**Figure 3c**). This implies that besides the presence of P sites, the crystal and electronic structure of each compound plays an important role by modifying the Ni surface states via Ni-Si and Ni-P bonding. The Tafel slope, b, is an indicator to evaluate the HER kinetics of electrocatalysts, given by the equation $\eta = a + b \times \log(j)$. The comparison of Tafel slopes showed that the ternary Ni_2SiP cathode exhibited the smallest value of $b = 80$ mV/dec in comparison with $b = 110$ mV/dec for binary Ni_5P_4 cathode (**Figure 3b**), indicating that Ni_2SiP has the smallest kinetic barrier for acidic HER. The Nyquist plots derived by EIS measurements also showed that Ni_2SiP has the smallest charge transfer resistance value of $R_{ct} = 9.2\ \Omega$, supporting the activity trend of $NiSi_{1-x}P_x$ cathodes (**Figure 3d**, **Table S3**).

The geometric double-layer capacitance (C_{dl}) of the cathodes was calculated using CV measurements with difference scan rates to estimate the electrochemical surface area (ECSA) (**Figures 3e and S17, Table S4**).[13,45,60] The results showed that Ni_5P_4 had the highest C_{dl} value of 117 mF/cm^2, followed by Ni_2SiP with $C_{dl} =$ 77.7 mF/cm^2. The polarization curves normalized by ECSA showed that Ni_2SiP still had the lowest $\eta_{10(ESCA)}$ value, 122 mV, while Ni_5P_4 had higher $\eta_{10(ESCA)}$ of 153 mV (**Figure S16**). The calculated turn-over frequncy (TOF) showed that the Ni_2SiP electrocatalyst had 66% higher TOF at 100 mV (vs RHE) than Ni_5P_4 (**Table S5**).

Accelerated degradation testing (ADT) and chronopotentiometry (CP) were performed to investigate the stability and durability of $NiSi_{1-x}P_x$ and Ni_5P_4 cathodes during acidic HER. **Figure 3f** shows the cycle-dependent cathodic polarization curves, and the results of the ADT experiments reveal that Ni_2SiP exhibited little difference in the η_{10} values or overall curvature after consecutive 1,000 CV cycles while Ni_5P_4 showed a noticeable increase in the η_{10} value, indicating better stability of Ni_2SiP. The same test of $Ni_5Si_2P_3$ and Ni_3SiP_2 showed almost no difference in η_{10} between the 1st and 1000th CV cycles (**Figure S18**). In turn, $Ni_7Si_2P_5$ showed signs of degradation like Ni_5P_4 (**Figures S19, 3f**). Similar trends were obtained from CP testing while tracing the η_{10} values for 20 h (**Figure 4, Table S6**). The ternary Ni_2SiP cathode exhibited stable activity in acidic HER (increasing η_{10} rate: ≈0.26 mV/h, 4.7% increase after 20 h) while the binary

Ni_5P_4 cathode displayed a considerable drop in overpotential (increasing η_{10} rate: ≈1.26 mV/h, 24.0% increase after 20 h), suggesting the superior stability of ternary Ni_2SiP as compared to Si-free binary Ni_5P_4. $Ni_5Si_2P_3$ and Ni_3SiP_2 showed a small decrease in activity, while $Ni_7Si_2P_5$ showed a considerable increase in overpotential. After the stability test, the powder XRD and SEM/EDS investigations reveal no substantial changes in the phase compositions and crystallinity of the spent $NiSi_{1-x}P_x$ electrocatalyst **(Figures S5, S7, and S8)**. For the $NiSi_{1-x}P_x$ electrocatalysts, stability increases with increasing Si content, and correspondingly, the number of Ni-Si bonds in the crystal structure. Ni-Si bonds are less polar than the Ni-P ones, due to the similar Pauling electronegativities of Ni (1.91) and Si (1.90) in contrast to that of P (2.19). ICP-MS results showed that the amount of Ni in the spent electrolyte was 0.098 mg for Ni_5P_4 and 0.145 mg for Ni_2SiP after 3 days of HER tests. In both cases the Ni leaching was less than 0.5% of the total Ni amount in the catalysts. The quantity of a leaching amount of Ni per generated mol of H_2 was 63.4 mg/mol for Ni_5P_4 and 49.1 mg/mol for Ni_2SiP, suggesting that Ni_2SiP exhibits lower Ni leaching for the same amount of hydrogen production (**Table S7**).

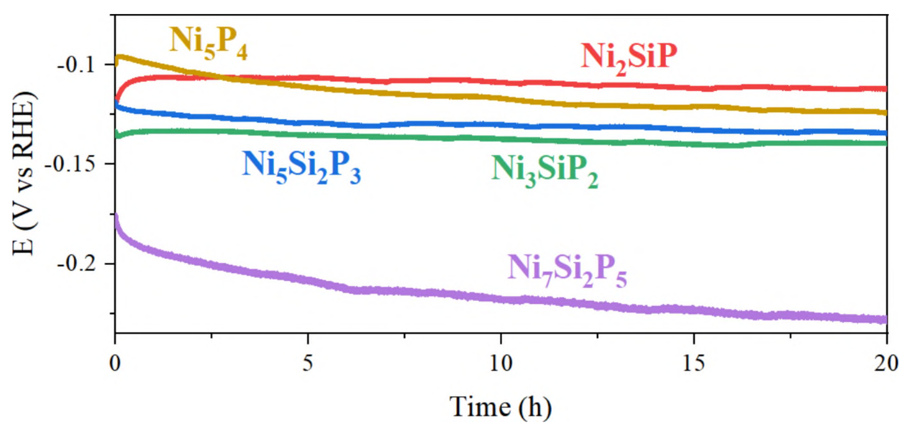

Figure 4. Continuous chronopotentiometric (CP) profiles at constant current density $j = -10$ mA/cm^2 for $NiSi_{1-x}P_x$ and Ni_5P_4 electrocatalysts. All recorded in 0.5M H_2SO_4 at room temperature.

From the point of view of practical applications, the stability and durability of the electrocatalyst is even more important than the value of the required overpotential. Water electrolyzers are expected to operate for years and even low degradation rates may lead to significant shortening of the electrolyzer uninterrupted operation time. As demonstrated here, our method for modifying phosphide electrocatalysts by introducing Si has a potential for real-life applications when combined with the scalable synthetic method capable of producing multigram quantities.

DFT Calculations

The experimental acidic HER activity of ternary $NiSi_{1-x}P_x$ cathodes was not directly proportional to the number of P atoms but instead showed the opposite relationship, in which higher P content phases had lower activity. Provided that any ternary $NiSi_{1-x}P_x$ electrocatalyst is significantly more active than P-free binary NiSi, the specific activity of the $NiSi_{1-x}P_x$ can be related to the electronic structure. The calculated total density of states (**Figure 5a**) showed that Ni_2SiP, $Ni_5Si_2P_3$, and $Ni_7Si_2P_5$ were metallic, and the number of states at the Fermi energy (E_F) increased with increasing Si content, where Ni_2SiP exhibited the highest and $Ni_7Si_2P_5$ had the lowest DOS at the E_F. In this regard, Si plays an important role in modulating the electronic structure of ternary $NiSi_{1-x}P_x$ catalysts. Interestingly, the increase in the density-of-states (DOS) at the E_F corresponds to an increase in the HER activity of the electrocatalysts (**Figure 5b**). This finding agrees with other experimental observations that a partial replacement of S or Se with a more electropositive P in CoS_2/$CoSe_2$ leads to an alteration of the DOS near the E_F and enhances the electrocatalytic activity.[32,71–73] The higher number of states at E_F enhances the HER activity of Ni_2SiP over that of P-rich ternary Ni–Si–P catalysts despite the fewer number of P active sites. While P was shown to be crucial as an adsorption site for hydrogen, Ni 3*d*-orbitals should also be involved in the electrocatalytic HER process. The overall increase of the number of states near E_F is achieved due to increased contribution of Ni 3*d* t_{2g} and e_g orbitals (shown in the partial DOS) while Si and P 3*p* contributions diminish with increasing Si content (**Figures 5c-f**). The analysis of Ni-Si and Ni-P interactions by means of COHP revealed that Ni_2SiP exhibited stronger bonding overlap at the l–2 to –3 eV range compared to that for $Ni_5Si_2P_3$ and $Ni_7Si_2P_5$ (**Figure S22**). Simultaneously, weak antibonding Ni-Si states are present at the E_F for Ni_2SiP which are diminished for $Ni_5Si_2P_3$ and $Ni_7Si_2P_5$. This suggests that the presence of Si may not only act as a stabilizer for the structure but also enhance the Ni orbital overlap with hydrogen, potentially leading to improved performance.[74] Thus, the superior properties of the Ni_2SiP electrocatalyst towards acidic HER are due to a synergistic combination of P active sites for H adsorption, a high DOS at the Fermi energy due to Ni 3*d* orbitals, and the enhanced stability due to high number of covalent Ni–Si bonds.

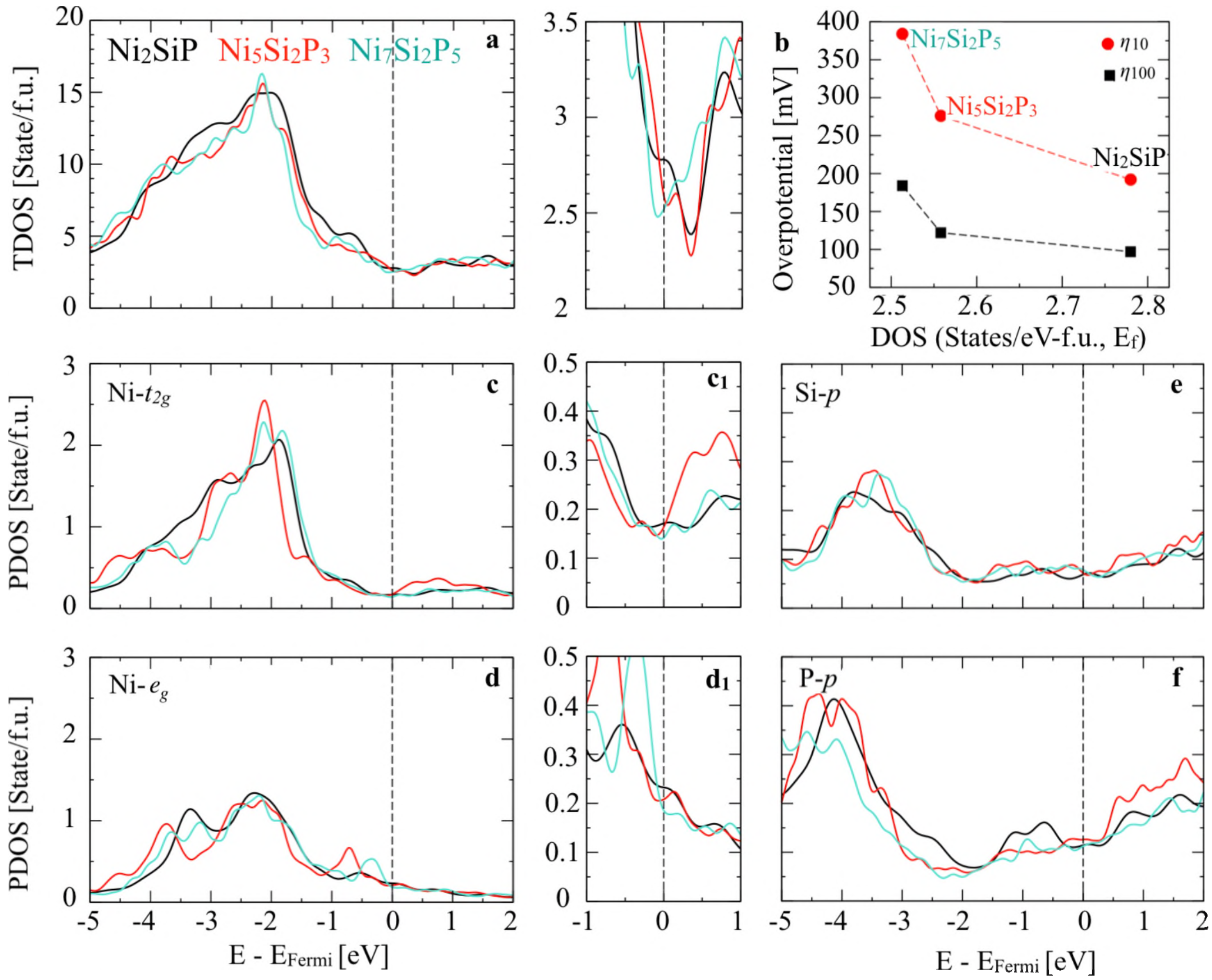

Figure 5. (a) Total density of states (TDOS) of ternary Ni_2SiP (black), $Ni_5Si_2P_3$ (red), and $Ni_7Si_2P_5$ (cyan) ordered structures. The zoomed DOS near the Fermi energy E_F are shown for clarity on the right hand-side. (b) Trend between the overpotential of the electrocatalysts and the DOS at E_F. Partial DOS (PDOS) of (c) t_{2g} and (d) e_g of Ni-3*d* bands and (e) Si-3*p* and (f) P-3*p* bands. The electronic structure (PDOS and bands) and bonding analysis of NiSi, $NiSi_{1-x}P_x$, and hypothetical NiP are shown in **Figures S20-S22**.

CONCLUSIONS

We showed that introducing a second non-metal element into transition-metal phosphides may be a viable strategy for developing a better HER electrocatalyst. By comparing NiSi and Ni_2SiP compounds with similar Ni oxidation states, we demonstrated that P sites are required to yield HER-active electrocatalysts. From the perspective of transition metal phosphides, a substantial part of P (up to 50%) may be replaced with a less active element, such as Si. Incorporation of Si resulted in the alteration of the electronic structure of the material allowing us to tune the catalytic activity. Formation of covalent Ni-Si bonds (which are less polar than Ni-P ones) resulted in an increased catalytic stability of the ternary Ni_2SiP phase. Similar effects have been observed when introducing the more electropositive Al into Ni phosphides [37,75] Ni_2SiP outperformed the state-of-the-art Ni_5P_4 catalyst in terms of activity and stability, when prepared and measured in the identical conditions.

Acknowledgments

We thank Dr. Simon R. Bare (SSRL) for his support in the measurement of XAS and data interpretation, Dr. Julia V. Zaikina (ISU) for access to the Spark Plasma Sintering machine, and Dr. Dmitri Y. Petrovykh and Dr. Oleksandr Bondarchuk (INL) for helping with the XPS measurements.

Funding Sources

Authors (S.K., G.V., E.S., M.A., D.D.J., K.K.) acknowledge the major research support for this project by the National Science Foundation under Grant No. 1955456. G.A. is grateful to the Ames National Laboratory Spedding Postdoctoral Fellowship for financial support. The work at Ames National Laboratory (P.S., G.A.) was supported by DOE Office of Science, Basic Energy Sciences, Materials Science & Engineering Division. The Ames National Laboratory is operated for the U.S. DOE by Iowa State University under contract #DE-AC02-07CH11358. Use of the Stanford Synchrotron Radiation Lightsource, SLAC National Accelerator Laboratory, is supported by the U.S. Department of Energy, Office of Science, Office of Basic Energy Sciences under Contract No. DE-AC02-76SF00515.

Supporting Information

The Supporting Information is available free of charge: Additional figures pertaining to powder X-ray diffraction, scanning electron microscopy, energy dispersive X-ray spectroscopy, X-ray photoelectron spectroscopy, X-ray absorption spectroscopy, electronic structure calculations, and HER tests.

AUTHOR INFORMATION

Corresponding Author

kovnir@iastate.edu

Notes

The authors declare no competing financial interest. The manuscript was written with the contribution of all authors.

REFERENCES

(1) Mazloomi, K.; Gomes, C. Hydrogen as an Energy Carrier: Prospects and Challenges. *Renew. Sustain. Energy Rev.* **2012**, *16* (5), 3024–3033.

(2) Serov, A.; Kovnir, K.; Shatruk, M.; Kolen'ko, Y. V. Critical Review of Platinum Group Metal-Free Materials for Water Electrolysis: Transition from the Laboratory to the Market : Earth-Abundant Borides and Phosphides as Catalysts for Sustainable Hydrogen Production. *Johns. Matthey Technol. Rev.* **2021**, *65* (2), 207–226.

(3) Liu, P.; Rodriguez, J. A. Catalysts for Hydrogen Evolution from the [NiFe] Hydrogenase to the $Ni_2P(001)$ Surface: The Importance of Ensemble Effect. *J. Am. Chem. Soc.* **2005**, *127* (42), 14871–14878.

(4) Popczun, E. J.; McKone, J. R.; Read, C. G.; Biacchi, A. J.; Wiltrout, A. M.; Lewis, N. S.; Schaak, R. E. Nanostructured Nickel Phosphide as an Electrocatalyst for the Hydrogen Evolution Reaction. *J. Am. Chem. Soc.* **2013**, *135* (25), 9267–9270.

(5) Wang, Y.; Kong, B.; Zhao, D.; Wang, H.; Selomulya, C. Strategies for Developing Transition Metal Phosphides as Heterogeneous Electrocatalysts for Water Splitting. *Nano Today* **2017**, *15*, 26–55.

(6) Sabatier, P. Hydrogénations et Déshydrogénations Par Catalyse. *Berichte Dtsch. Chem. Ges.* **1911**, *44* (3), 1984–2001.

(7) Owens-Baird, B.; Kolen'ko, Y. V.; Kovnir, K. Structure–Activity Relationships for Pt-Free Metal Phosphide Hydrogen Evolution Electrocatalysts. *Chem. – Eur. J.* **2018**, *24* (29), 7298–7311.

(8) Kibsgaard, J.; Tsai, C.; Chan, K.; Benck, J. D.; Nørskov, J. K.; Abild-Pedersen, F.; Jaramillo, T. F. Designing an Improved Transition Metal Phosphide Catalyst for Hydrogen Evolution Using Experimental and Theoretical Trends. *Energy Environ. Sci.* **2015**, *8* (10), 3022–3029.

(9) Ha, D.-H.; Han, B.; Risch, M.; Giordano, L.; Yao, K. P. C.; Karayaylali, P.; Shao-Horn, Y. Activity and Stability of Cobalt Phosphides for Hydrogen Evolution upon Water Splitting. *Nano Energy* **2016**, *29*, 37–45.

(10) Wexler, R. B.; Martirez, J. M. P.; Rappe, A. M. Active Role of Phosphorus in the Hydrogen Evolving Activity of Nickel Phosphide (0001) Surfaces. *ACS Catal.* **2017**, *7* (11), 7718–7725.

(11) Laursen, A. B.; Wexler, R. B.; Whitaker, M. J.; Izett, E. J.; Calvinho, K. U. D.; Hwang, S.; Rucker, R.; Wang, H.; Li, J.; Garfunkel, E.; Greenblatt, M.; Rappe, A. M.; Dismukes, G. C. Climbing the Volcano of Electrocatalytic Activity While Avoiding Catalyst Corrosion: Ni_3P, a Hydrogen Evolution Electrocatalyst Stable in Both Acid and Alkali. *ACS Catal.* **2018**, *8* (5), 4408–4419.

(12) Owens-Baird, B.; Sousa, J. P. S.; Ziouani, Y.; Petrovykh, D. Y.; Zarkevich, N. A.; Johnson, D. D.; Kolen'ko, Y. V.; Kovnir, K. Crystallographic Facet Selective HER Catalysis: Exemplified in FeP and NiP_2 Single Crystals. *Chem. Sci.* **2020**, *11* (19), 5007–5016.

(13) Duan, J.; Chen, S.; Ortíz-Ledón, C. A.; Jaroniec, M.; Qiao, S. Phosphorus Vacancies That Boost Electrocatalytic Hydrogen Evolution by Two Orders of Magnitude. *Angew. Chem. Int. Ed.* **2020**, *59* (21), 8181–8186.

(14) He, Y.; Wang, T.; Zhang, M.; Wang, T.; Wu, L.; Zeng, L.; Wang, X.; Boubeche, M.; Wang, S.; Yan, K.; Lin, S.; Luo, H. Discovery and Facile Synthesis of a New Silicon Based Family as Efficient Hydrogen Evolution Reaction Catalysts: A Computational and Experimental Investigation of Metal Monosilicides. *Small* **2021**, *17* (8), 2006153.

(15) Zhang, J.; Zhang, Z.; Ji, Y.; Yang, J.; Fan, K.; Ma, X.; Wang, C.; Shu, R.; Chen, Y. Surface Engineering Induced Hierarchical Porous $Ni_{12}P_5$-Ni_2P Polymorphs Catalyst for Efficient Wide PH Hydrogen Production. *Appl. Catal. B Environ.* **2021**, *282*, 119609.

(16) Laursen, A. B.; Patraju, K. R.; Whitaker, M. J.; Retuerto, M.; Sarkar, T.; Yao, N.; Ramanujachary, K. V.; Greenblatt, M.; Dismukes, G. C. Nanocrystalline Ni_5P_4: A Hydrogen Evolution Electrocatalyst of Exceptional Efficiency in Both Alkaline and Acidic Media. *Energy Environ. Sci.* **2015**, *8* (3), 1027–1034.

(17) Owens-Baird, B.; Xu, J.; Petrovykh, D. Y.; Bondarchuk, O.; Ziouani, Y.; González-Ballesteros, N.; Yox, P.; Sapountzi, F. M.; Niemantsverdriet, H.; Kolen'ko, Y. V.; Kovnir, K. NiP_2: A Story of Two Divergent Polymorphic Multifunctional Materials. *Chem. Mater.* **2019**, *31* (9), 3407–3418.

(18) Dera, P.; Lazarz, J. D.; Lavina, B. Pressure-Induced Development of Bonding in NiAs Type Compounds and Polymorphism of NiP. *J. Solid State Chem.* **2011**, *184* (8), 1997–2003.

(19) Dera, P.; Nisar, J.; Ahuja, R.; Tkachev, S.; Prakapenka, V. B. New Type of Possible High-Pressure Polymorphism in NiAs Minerals in Planetary Cores. *Phys. Chem. Miner.* **2013**, *40* (2), 183–193.

(20) Il'nitskaya, O. N.; Kuz'ma, Yu. B.; Fundamentskii, V. S. New Compound Ni_2SiP and Its Crystal Structure. *Dokl. Akad Nauk Ukr SSR Ser* **1989**, *9*, 81–83.

(21) llnitskaya, O. N.; Kuz'ma, Yu. B.; Fundamentskii, V. S. Crystal Chemistry of Series of Nonuniform Linear Stuructures. The Series of Nonuniform Linear Sructure $M_{2m+2n}X_{2m+2n}$ and Its New Representative $Ni_5Si_2P_3$. *Kristallografia* **1992**, *37*, 146–150.

(22) llnitskaya, O. N.; Kuz'ma, Yu. B. The Reaction of Nickel with Silicon and Phosphorus. *Russ J Inorg Chem* **1992**, *37*, 700–702.

(23) Oryshchyn, S. V.; Babizhets'ky, V. S.; Kuz'ma, Yu. B.; Głowiak, T. Preparation and Crystal Structure of the $Ni_7Si_2P_5$ Phosphide. *Z. Für Krist.* **1999**, *214* (6), 337–340.

(24) El-Refaei, S. M.; Russo, P. A.; Pinna, N. Recent Advances in Multimetal and Doped Transition-Metal Phosphides for the Hydrogen Evolution Reaction at Different PH Values. *ACS Appl. Mater. Interfaces* **2021**, *13* (19), 22077–22097.

(25) Wang, Q.; He, R.; Yang, F.; Tian, X.; Sui, H.; Feng, L. An Overview of Heteroatom Doped Cobalt Phosphide for Efficient Electrochemical Water Splitting. *Chem. Eng. J.* **2023**, *456*, 141056.

(26) Zhou, Q.; Shen, Z.; Zhu, C.; Li, J.; Ding, Z.; Wang, P.; Pan, F.; Zhang, Z.; Ma, H.; Wang, S.; Zhang, H. Nitrogen-Doped CoP Electrocatalysts for Coupled Hydrogen Evolution and Sulfur Generation with Low Energy Consumption. *Adv. Mater.* **2018**, *30* (27), 1800140.

(27) Wang, L.; Wu, H.; Xi, S.; Chua, S. T.; Wang, F.; Pennycook, S. J.; Yu, Z. G.; Du, Y.; Xue, J. Nitrogen-Doped Cobalt Phosphide for Enhanced Hydrogen Evolution Activity. *ACS Appl. Mater. Interfaces* **2019**, *11* (19), 17359–17367.

(28) Men, Y.; Li, P.; Zhou, J.; Cheng, G.; Chen, S.; Luo, W. Tailoring the Electronic Structure of Co_2P by N Doping for Boosting Hydrogen Evolution Reaction at All PH Values. *ACS Catal.* **2019**, *9* (4), 3744–3752.

(29) Zhou, G.; Li, M.; Li, Y.; Dong, H.; Sun, D.; Liu, X.; Xu, L.; Tian, Z.; Tang, Y. Regulating the Electronic Structure of CoP Nanosheets by O Incorporation for High-Efficiency Electrochemical Overall Water Splitting. *Adv. Funct. Mater.* **2020**, *30* (7), 1905252.

(30) Xu, K.; Sun, Y.; Li, X.; Zhao, Z.; Zhang, Y.; Li, C.; Fan, H. J. Fluorine-Induced Dual Defects in Cobalt Phosphide Nanosheets Enhance Hydrogen Evolution Reaction Activity. *ACS Mater. Lett.* **2020**, *2* (7), 736–743.

(31) Kibsgaard, J.; Jaramillo, T. F. Molybdenum Phosphosulfide: An Active, Acid-Stable, Earth-Abundant Catalyst for the Hydrogen Evolution Reaction. *Angew. Chem.* **2014**, *126* (52), 14661–14665.

(32) Cabán-Acevedo, M.; Stone, M. L.; Schmidt, J. R.; Thomas, J. G.; Ding, Q.; Chang, H.-C.; Tsai, M.-L.; He, J.-H.; Jin, S. Efficient Hydrogen Evolution Catalysis Using Ternary Pyrite-Type Cobalt Phosphosulphide. *Nat. Mater.* **2015**, *14* (12), 1245–1251.

(33) Chang, J.; Li, K.; Wu, Z.; Ge, J.; Liu, C.; Xing, W. Sulfur-Doped Nickel Phosphide Nanoplates Arrays: A Monolithic Electrocatalyst for Efficient Hydrogen Evolution Reactions. *ACS Appl. Mater. Interfaces* **2018**, *10* (31), 26303–26311.

(34) Zhuo, J.; Cabán-Acevedo, M.; Liang, H.; Samad, L.; Ding, Q.; Fu, Y.; Li, M.; Jin, S. High-Performance Electrocatalysis for Hydrogen Evolution Reaction Using Se-Doped Pyrite-Phase Nickel Diphosphide Nanostructures. *ACS Catal.* **2015**, *5* (11), 6355–6361.

(35) Chu, Y.-C.; Chang, C.-J.; Zhu, Y.; Lin, S.-C.; Tung, C.-W.; Chen, T.-L.; Chen, H. M. Anionic Effects on Metal Pair of Se-Doped Nickel Diphosphide for Hydrogen Evolution Reaction. *ACS Sustain. Chem. Eng.* **2019**, *7* (16), 14247–14255.

(36) Men, Y.; Tan, Y.; Li, P.; Cao, X.; Jia, S.; Wang, J.; Chen, S.; Luo, W. Tailoring the 3d-Orbital Electron Filling Degree of Metal Center to Boost Alkaline Hydrogen Evolution Electrocatalysis. *Appl. Catal. B Environ.* **2021**, *284*, 119718.

(37) Lado, J. L.; Wang, X.; Paz, E.; Carbó-Argibay, E.; Guldris, N.; Rodríguez-Abreu, C.; Liu, L.; Kovnir, K.; Kolen'ko, Y. V. Design and Synthesis of Highly Active Al–Ni–P Foam Electrode for Hydrogen Evolution Reaction. *ACS Catal.* **2015**, *5* (11), 6503–6508.

(38) Zhang, R.; Tang, C.; Kong, R.; Du, G.; Asiri, A. M.; Chen, L.; Sun, X. Al-Doped CoP Nanoarray: A Durable Water-Splitting Electrocatalyst with Superhigh Activity. *Nanoscale* **2017**, *9* (14), 4793–4800.

(39) Cao, E.; Chen, Z.; Wu, H.; Yu, P.; Wang, Y.; Xiao, F.; Chen, S.; Du, S.; Xie, Y.; Wu, Y.; Ren, Z. Boron-Induced Electronic-Structure Reformation of CoP Nanoparticles Drives Enhanced PH-Universal Hydrogen Evolution. *Angew. Chem. Int. Ed.* **2020**, *59* (10), 4154–4160.

(40) Shi, Y.; Zhang, B. Recent Advances in Transition Metal Phosphide Nanomaterials: Synthesis and Applications in Hydrogen Evolution Reaction. *Chem. Soc. Rev.* **2016**, *45* (6), 1529–1541.

(41) Park, H.; Zhang, Y.; Lee, E.; Shankhari, P.; Fokwa, B. P. T. High-Current-Density HER Electrocatalysts: Graphene-like Boron Layer and Tungsten as Key Ingredients in Metal Diborides. *ChemSusChem* **2019**, *12* (16), 3726–3731.

(42) Toby, B. H.; Von Dreele, R. B. *GSAS-II* : The Genesis of a Modern Open-Source All Purpose Crystallography Software Package. *J. Appl. Crystallogr.* **2013**, *46* (2), 544–549.

(43) Ravel, B.; Newville, M. *ATHENA* , *ARTEMIS* , *HEPHAESTUS* : Data Analysis for X-Ray Absorption Spectroscopy Using *IFEFFIT*. *J. Synchrotron Radiat.* **2005**, *12* (4), 537–541.

(44) McCrory, C. C. L.; Jung, S.; Peters, J. C.; Jaramillo, T. F. Benchmarking Heterogeneous Electrocatalysts for the Oxygen Evolution Reaction. *J. Am. Chem. Soc.* **2013**, *135* (45), 16977–16987.

(45) Zhou, D.; He, L.; Zhu, W.; Hou, X.; Wang, K.; Du, G.; Zheng, C.; Sun, X.; Asiri, A. M. Interconnected Urchin-like Cobalt Phosphide Microspheres Film for Highly Efficient Electrochemical Hydrogen Evolution in Both Acidic and Basic Media. *J. Mater. Chem. A* **2016**, *4* (26), 10114–10117.

(46) Kresse, G.; Hafner, J. Norm-Conserving and Ultrasoft Pseudopotentials for First-Row and Transition Elements. *J. Phys. Condens. Matter* **1994**, *6* (40), 8245–8257.

(47) Hafner, J. *Ab-Initio* Simulations of Materials Using VASP: Density-Functional Theory and Beyond. *J. Comput. Chem.* **2008**, *29* (13), 2044–2078.

(48) Perdew, J. P.; Burke, K.; Ernzerhof, M. Generalized Gradient Approximation Made Simple. *Phys. Rev. Lett.* **1996**, *77* (18), 3865–3868.

(49) Maintz, S.; Deringer, V. L.; Tchougréeff, A. L.; Dronskowski, R. Analytic Projection from Plane-Wave and PAW Wavefunctions and Application to Chemical-Bonding Analysis in Solids. *J. Comput. Chem.* **2013**, *34* (29), 2557–2567.

(50) Maintz, S.; Deringer, V. L.; Tchougréeff, A. L.; Dronskowski, R. LOBSTER: A Tool to Extract Chemical Bonding from Plane-Wave Based DFT: Tool to Extract Chemical Bonding. *J. Comput. Chem.* **2016**, *37* (11), 1030–1035.

(51) Dronskowski, R.; Bloechl, P. E. Crystal Orbital Hamilton Populations (COHP): Energy-Resolved Visualization of Chemical Bonding in Solids Based on Density-Functional Calculations. *J. Phys. Chem.* **1993**, *97* (33), 8617–8624.

(52) Hoffmann, R. *Solids and Surfaces: A Chemist's View of Bonding in Extended Structures*; VCH publishers Inc., New York, 1998.

(53) Dronskowski, R. *Computational Chemistry of Solid State Materials*; Wiley-VCH, Weinheim, New York, 2005.

(54) Lee, S. J.; Won, J.; Wang, L.; Jing, D.; Harmer, C. P.; Mark, J.; Akopov, G.; Kovnir, K. New Noncentrosymmetric Tetrel Pnictides Composed of Square-Planar Gold(I) with Peculiar Bonding. *Chem. – Eur. J.* **2021**, *27* (26), 7383–7390.

(55) Akopov, G.; Hewage, N. W.; Yox, P.; Viswanathan, G.; Lee, S. J.; Hulsebosch, L. P.; Cady, S. D.; Paterson, A. L.; Perras, F. A.; Xu, W.; Wu, K.; Mudryk, Y.; Kovnir, K. Synthesis-Enabled Exploration of Chiral and Polar Multivalent Quaternary Sulfides. *Chem. Sci.* **2021**, *12* (44), 14718–14730.

(56) Akopov, G.; Mark, J.; Viswanathan, G.; Lee, S. J.; McBride, B. C.; Won, J.; Perras, F. A.; Paterson, A. L.; Yuan, B.; Sen, S.; Adeyemi, A. N.; Zhang, F.; Wang, C.-Z.; Ho, K.-M.; Miller, G. J.; Kovnir, K. Third Time's the Charm: Intricate Non-Centrosymmetric Polymorphism in LnSiP$_3$ (Ln = La and Ce) Induced by Distortions of Phosphorus Square Layers. *Dalton Trans.* **2021**, *50* (19), 6463–6476.

(57) Lee, S. J.; Viswanathan, G.; Carnahan, S. L.; Harmer, C. P.; Akopov, G.; Rossini, A. J.; Miller, G. J.; Kovnir, K. Add a Pinch of Tetrel: The Transformation of a Centrosymmetric Metal into a Nonsymmorphic and Chiral Semiconductor. *Chem. – Eur. J.* **2022**, *28* (9), e202104319.

(58) Akopov, G.; Viswanathan, G.; Hewage, N. W.; Yox, P.; Wu, K.; Kovnir, K. Pd and Octahedra Do Not Get along: Square Planar [PdS_4] Units in Non-Centrosymmetric $La_6PdSi_2S_{14}$. *J. Alloys Compd.* **2022**, *902*, 163756.

(59) Akopov, G.; Hewage, N. W.; Viswanathan, G.; Yox, P.; Wu, K.; Kovnir, K. Non-Linear Optical Properties of the $(RE)_3CuGeS_7$ Family of Compounds. *Z. Für Anorg. Allg. Chem.* **2022**, *648* (15), e202200096.

(60) Fu, Q.; Wang, X.; Han, J.; Zhong, J.; Zhang, T.; Yao, T.; Xu, C.; Gao, T.; Xi, S.; Liang, C.; Xu, L.; Xu, P.; Song, B. Phase-Junction Electrocatalysts towards Enhanced Hydrogen Evolution Reaction in Alkaline Media. *Angew. Chem. Int. Ed.* **2021**, *60* (1), 259–267.

(61) Blanchard, P. E. R.; Grosvenor, A. P.; Cavell, R. G.; Mar, A. X-Ray Photoelectron and Absorption Spectroscopy of Metal-Rich Phosphides M_2P and M_3P (M = Cr−Ni). *Chem. Mater.* **2008**, *20* (22), 7081–7088.

(62) Tam, P. L.; Nyborg, L. Sputter Deposition and XPS Analysis of Nickel Silicide Thin Films. *Surf. Coat. Technol.* **2009**, *203* (19), 2886–2890.

(63) Cao, Y.; Nyborg, L.; Jelvestam, U. XPS Calibration Study of Thin-Film Nickel Silicides. *Surf. Interface Anal.* **2009**, *41* (6), 471–483.

(64) Saadi, F. H.; Carim, A. I.; Drisdell, W. S.; Gul, S.; Baricuatro, J. H.; Yano, J.; Soriaga, M. P.; Lewis, N. S. *Operando* Spectroscopic Analysis of CoP Films Electrocatalyzing the Hydrogen-Evolution Reaction. *J. Am. Chem. Soc.* **2017**, *139* (37), 12927–12930.

(65) Naftel, S. J.; Coulthard, I.; Sham, T. K.; Das, S. R.; Xu, D.-X. Structural and Electronic Property Evolution of Nickel and Nickel Silicide Thin Films on Si(100) from Multicore x-Ray-Absorption Fine-Structure Studies. *Phys. Rev. B* **1998**, *57* (15), 9179–9185.

(66) Fujita, S.; Nakajima, K.; Yamasaki, J.; Mizugaki, T.; Jitsukawa, K.; Mitsudome, T. Unique Catalysis of Nickel Phosphide Nanoparticles to Promote the Selective Transformation of Biofuranic Aldehydes into Diketones in Water. *ACS Catal.* **2020**, *10* (7), 4261–4267.

(67) Al Rashid, M. H.; Dipu, A. L.; Nishikawa, Y.; Ogihara, H.; Inami, Y.; Iguchi, S.; Yamanaka, I.; Nagamatsu, S.; Kido, D.; Hu, B.; Asakura, K. X-Ray Absorption Fine Structure Studies on Nickel Phosphide Catalysts for the Non-Oxidative Coupling of Methane Reaction Using a Theoretical Model. *Radiat. Phys. Chem.* **2021**, *189*, 109727.

(68) Toman, K. The Structure of NiSi. *Acta Crystallogr.* **1951**, *4*, 462–464.

(69) Vijh, A. K.; Bélanger, G.; Jacques, R. Electrochemical Activity of Silicides of Some Transition Metals for the Hydrogen Evolution Reaction in Acidic Solutions. *Int. J. Hydrog. Energy* **1990**, *15* (11), 789–794.

(70) Mittermeier, T.; Madkikar, P.; Wang, X.; Gasteiger, H.; Piana, M. Probing Transition-Metal Silicides as PGM-Free Catalysts for Hydrogen Oxidation and Evolution in Acidic Medium. *Materials* **2017**, *10* (6), 661.

(71) Anjum, M. A. R.; Okyay, M. S.; Kim, M.; Lee, M. H.; Park, N.; Lee, J. S. Bifunctional Sulfur-Doped Cobalt Phosphide Electrocatalyst Outperforms All-Noble-Metal Electrocatalysts in Alkaline Electrolyzer for Overall Water Splitting. *Nano Energy* **2018**, *53*, 286–295.

(72) Zhang, R.; Huang, J.; Chen, G.; Chen, W.; Song, C.; Li, C.; Ostrikov, K. In Situ Engineering Bi-Metallic Phospho-Nitride Bi-Functional Electrocatalysts for Overall Water Splitting. *Appl. Catal. B Environ.* **2019**, *254*, 414–423.

(73) Zheng, Y.-R.; Wu, P.; Gao, M.-R.; Zhang, X.-L.; Gao, F.-Y.; Ju, H.-X.; Wu, R.; Gao, Q.; You, R.; Huang, W.-X.; Liu, S.-J.; Hu, S.-W.; Zhu, J.; Li, Z.; Yu, S.-H. Doping-Induced Structural Phase Transition in Cobalt Diselenide Enables Enhanced Hydrogen Evolution Catalysis. *Nat. Commun.* **2018**, *9* (1), 2533.

(74) Hammer, B.; Norskov, J. K. Why Gold Is the Noblest of All the Metals. *Nature* **1995**, *376* (6537), 238–240.

(75) Xu, J.; Sousa, J. P. S.; Mordvinova, N. E.; Costa, J. D.; Petrovykh, D. Y.; Kovnir, K.; Lebedev, O. I.; Kolen'ko, Y. V. Al-Induced In Situ Formation of Highly Active Nanostructured Water-Oxidation Electrocatalyst Based on Ni-Phosphide. *ACS Catal.* **2018**, *8* (3), 2595–2600.